JGR Space Physics

RESEARCH ARTICLE
10.1029/2020JA029043

Quiet Night Arctic Ionospheric *D* Region Characteristics

Neil R. Thomson[1], **Mark A. Clilverd**[2], **James B. Brundell**[1], **and Craig J. Rodger**[1]

[1]Physics Department, University of Otago, Dunedin, New Zealand, [2]British Antarctic Survey (UKRI-NERC), Cambridge, UK

Key Points:

- Arctic VLF radio propagation recordings enable the characteristics of the nighttime polar *D* region to be inferred
- The undisturbed night Arctic *D* region is more variable and occurs at lower altitudes (~78 km), than at lower latitudes (~85 km)
- The polar *D* region is maintained mainly by electron precipitation rather than by Lyman-alpha or galactic cosmic rays

Supporting Information:

Supporting Information may be found in the online version of this article.

Correspondence to:

N. R. Thomson,
thomsoneil@gmail.com

Citation:

Thomson, N. R., Clilverd, M. A., Brundell, J. B., & Rodger, C. J. (2021). Quiet night Arctic ionospheric *D* region characteristics. *Journal of Geophysical Research: Space Physics*, *126*, e2020JA029043. https://doi.org/10.1029/2020JA029043

Received 22 DEC 2020
Accepted 26 MAR 2021

Abstract VLF radio propagation recordings are used to determine the characteristics of the nighttime polar lower *D* region of the ionosphere. Recordings of both VLF phase and amplitude in the Arctic on days within ~1–2 weeks of the equinoxes enable their day-to-night changes to be determined. These changes are then combined with previously measured daytime polar *D* region characteristics to find the nighttime characteristics. The previously determined daytime characteristics were measured in the Arctic summer; the NRLMSISE atmosphere model is used to help determine the height change from daytime summer to daytime equinox (~5 km lower). The principal path used was from the 16.4 kHz Norwegian transmitter JXN (67°N, 14°E) 1,334 km northwards across the Arctic Ocean to Ny-Ålesund (79°N, 12°E), Svalbard. Also used were the 2,014-km path from NRK (37.5 kHz, Grindavik, 64°N, Iceland) to Ny-Ålesund, the 1,655-km path from JXN to Reykjavik (64°N, Iceland), and the 5,302-km path from JXN across the Arctic Ocean to Fairbanks (65°N) in Alaska. The night values of (the Wait parameters) H' and β were found to average from ~79 km at equinox down to 77 km near winter solstice (lower than the 85 km at low and midlatitudes by ~7 km) and 0.6 km^{-1}, respectively. This lower height and its variability are shown to be consistent with the principal source of ionization being energetic electron precipitation.

1. Introduction

The lowest region of the Earth's ionosphere (containing free electrons) is the *D* region with its lower edge at heights generally around 70 km by day and 85 km by night. These heights are too low for satellite measurements (too much drag) and too high for aircraft or balloons. Rocket measurements (e.g., Friedrich & Torkar, 2001; Friedrich et al., 2018) have proved very useful but tend to be too transient and expensive to fully explore the significant diurnal, seasonal, and latitudinal variations around the Earth. Ground-based, high frequency radars (e.g., Singer et al., 2011) have also proved useful when available but are quite rare and are very limited in their geographical coverage. In contrast, very low frequency (VLF) radio waves, particularly from single-frequency, ground-based, man-made transmitters, have good geographical coverage and very good (often continuous) diurnal and seasonal coverage. These waves readily partially reflect from the lower edge of the *D* region with the resulting amplitude and phase changes being rather sensitive to its height and sharpness. The VLF waves also reflect very well from the Earth's surface, particularly the conducting oceans, enabling them to travel up to large distances (thousands of km) in the Earth-ionosphere waveguide bounded above by the *D* region.

VLF radio subionospheric propagation has been used to refine our knowledge of the daytime *D* region by taking amplitude and phase measurements along radio paths both near (~100 km from) the transmitter, where the direct ground wave signal dominates, and at greater distances (from ~300 km up to several thousand km away) where the waves reflected from the *D* region dominate. The resulting phase and amplitude changes along the paths were then compared with calculations from VLF subionospheric modeling codes enabling the latitude-dependent characteristics (height and sharpness) of the daytime *D* region to be inferred, e.g., Thomson (2010) and Thomson et al. (2012, 2014) at low latitudes, Thomson et al. (2011, 2017) at midlatitudes, and Thomson et al. (2018) at high latitudes in the Arctic. The current study builds on these earlier studies to examine the nighttime Arctic *D* region.

Diurnal VLF radio propagation recordings have been used to find the characteristics of the nighttime *D* region of the ionosphere at lower latitudes on a variety of long paths by comparing the observed changes in phase and amplitude between day and night with calculations from VLF propagation codes (Thomson & McRae, 2009; Thomson et al., 2007). For these comparisons the daytime results of Thomson (1993) and McRae and Thomson (2000) were used. In the present paper, we again use single-frequency, diurnal

VLF recordings, but made in the Arctic, over nearly all-sea paths. We then determine the characteristics of the night Arctic *D* region by using the daytime Arctic results of Thomson et al. (2018) together with the measured day-night amplitude and phase changes from these Arctic VLF recordings, and then comparing with calculations from VLF propagation code for various candidate night *D*-region electron density profiles.

By day, the free electrons in the *D* region (which reflect the VLF radio waves) are generated at midlatitude and low latitude by solar Lyman-α, mainly above altitudes of ∼70 km, and galactic cosmic rays, mainly below ∼70 km (e.g., Thomson et al., 2017). Toward the poles, the solar Lyman-α becomes less significant because of the higher solar zenith angles, the galactic cosmic rays become more significant because of the reduced shielding of the Earth's magnetic field (e.g., Neal et al., 2015), and electron precipitation starts to become significant, tending to be dominant in the auroral regions (Thomson et al., 2018). By night, the lower (reflecting) edge of the *D* region at low and middle latitudes is higher ($H' \sim 85$ km) than by day ($H' \sim 70$ km) and is also more variable (Thomson & McRae, 2009; Thomson et al., 2007). Both by day and by night large quantities of free electrons are continuously removed by attachment to O_2 molecules at heights below ∼80 km: $O_2 + e^- \rightarrow O_2^-$ but this is effectively negated during the day by the electrons being immediately released again by visible light photons. This loss mechanism is rather height dependent because the scale height of neutral O_2 is only ∼6 km resulting in the free electron concentration below ∼80-km altitude becoming quite low at night. Also, of course, there is no direct solar Lyman-α radiation at night. However, reradiation of solar Lyman-α from the (atomic) hydrogen in the Earth's geocorona is an important, likely dominant, generation source for the quiet night *D* region at low and middle latitudes away from the polar regions; toward the polar regions galactic cosmic rays become significant. Electron precipitation from the radiation belts can also contribute at midlatitudes at least during disturbed times. Closer to the polar regions and particularly within the polar regions electron precipitation is likely to be a major contributor even at quiet times.

Here, we determine the characteristics of the lower edge of the quiet nighttime polar *D* region, in particular to find if there is evidence that the ionization is maintained significantly by electron precipitation even during quiet times. Of course the polar ionosphere is likely seldom, if ever, truly quiet. So, our quiet periods will in fact include the bulk of the observations but will exclude periods which are clearly significantly disturbed or likely to be so. The VLF propagation paths used here are shown in Figure 1. The three short (<∼2,000 km) nearly all-sea paths are shown in Figure 1a. These include the principal path here of JXN on 16.4 kHz from ∼67°N in Norway to ∼79°N at Ny-Ålesund, Svalbard, and the other two short paths, NRK (∼64°N, 37.5 kHz), Grindavik, Iceland, to Ny-Ålesund and JXN to Reykjavik, Iceland. Figure 1b shows the long (∼5,302 km), nearly all-sea path from JXN to Fairbanks (∼65°N), Alaska. Figure 1c shows the nonpolar path from NPM (∼21°N), Hawaii, to Fairbanks used in Section 4 to check the consistency of the gain of the Fairbanks antenna.

2. JXN (Norway) to Ny-Ålesund (Svalbard)

2.1. Observations

JXN is a VLF transmitter on the west coast of Norway near 66.98°N, 13.87°E which radiates, with stable phase and amplitude, at 16.4 kHz modulated with 200-baud MSK (minimum shift keying). The radiated power is ∼50 kW (Thomson et al., 2018) but the exact radiated power is not needed here because only the day-to-night differences in amplitude and phase are used; i.e., the night propagation parameters are measured relative to the previously measured daytime parameters as reported by Thomson et al. (2018). The signals from JXN are received 1,334 km to the north on a loop antenna at Ny-Ålesund (78.92°N, 11.93°E), Svalbard, where their amplitudes and phases (relative to GPS 1-s pulses) are continuously recorded using an UltraMSK receiver (http://ultramsk.com); the Ny-Ålesund receiver is part of the AARDDVARK network (Antarctic-Arctic Radiation-belt Dynamic Deposition VLF Atmospheric Research Konsortia: e.g., Clilverd et al., 2009, http://www.physics.otago.ac.nz/space/AARDDVARK_homepage.htm).

Figure 2 shows the diurnal variations of phase and amplitude of JXN observed at Ny-Ålesund for three representative equinoctial weeks, from top to bottom one each for March 2020, September 2019, and September 2018. Daytime at this longitude (∼13°E) can be seen to be ∼5–17 UT while night begins ∼21 UT

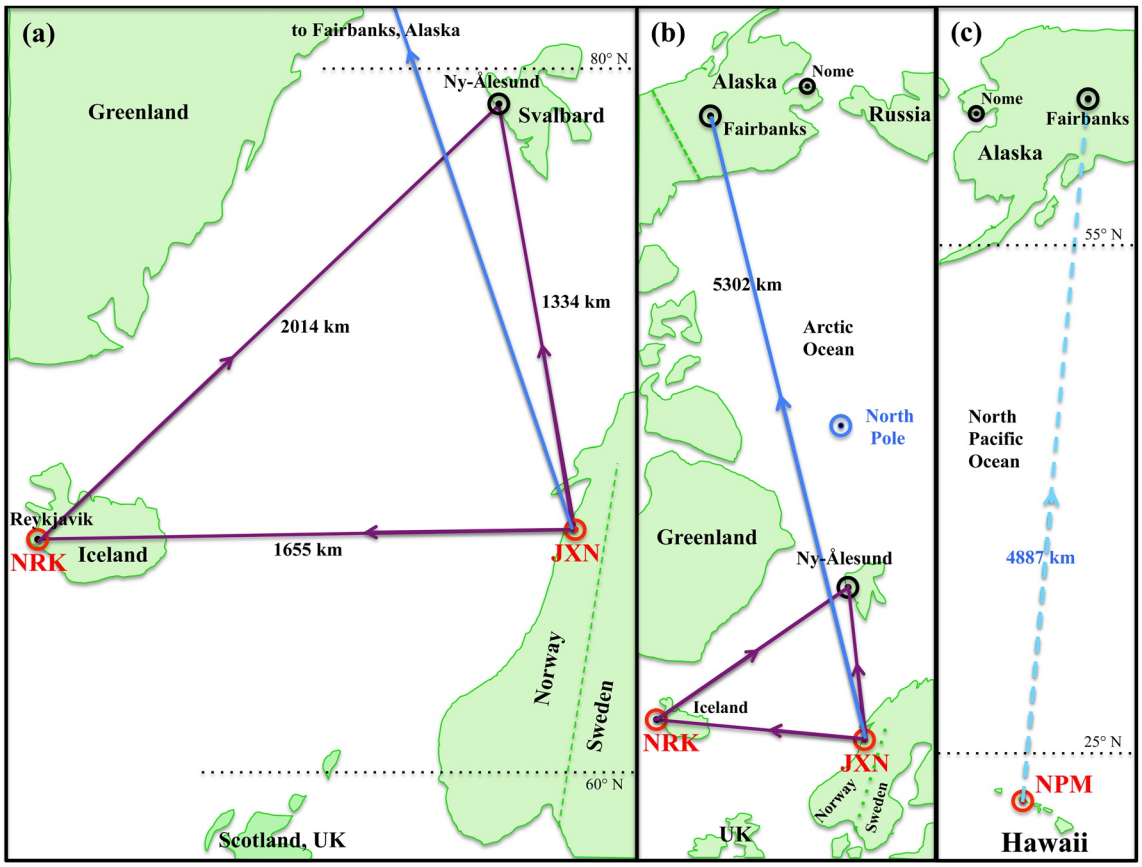

Figure 1. VLF radio paths used in this study. (a) Short paths in the Arctic: JXN (16.4 kHz, Norway) to both Ny-Ålesund (Svalbard) and Iceland, and NRK (37.5 kHz, Iceland) to Ny-Ålesund. (b) The long Arctic path JXN to Fairbanks (Alaska). (c) The (mainly) midlatitude path from NPM (21.4 kHz, Hawaii) to Fairbanks to monitor any variations in receiver antenna gain. VLF, very low frequency.

and ends ~2–3 UT, depending on whether the date is a little on the winter or summer side of equinox. For convenience and to avoid both the early settling of the night ionosphere and any premidnight disturbances, we have chosen to use the night results (phases and amplitudes) from 0 UT up to just before the dawn period starts, i.e., typically up to ~2–3 UT. During daytime, as can be seen in the plots, the amplitude and particularly the phase, in the absence of disturbances, vary remarkably little with time of day, i.e., with solar zenith angle, at these high solar zenith angles. This is consistent with polar, daytime generation of ionization being dominated by slowly varying precipitation or galactic cosmic rays rather than solar Lyman-α which dominates at lower latitudes (Thomson et al., 2018). As can be seen in the amplitude panel for September 23–29, 2019, the daytime amplitude is occasionally disturbed in only moderately active geomagnetic conditions; however, generally a quiet baseline amplitude is readily identified at about −42.0 dB (relative to a fixed but arbitrary level) in these amplitude plots, and this daytime baseline has been used here to record the day-night amplitude changes in dB. From the six panels in Figure 2, it can thus be seen that the day-night changes in phase and amplitude are ~60–70° and ~5–7 dB, respectively. Similar plots were also made for the remaining available equinoctial days between September 2014 and March 2020. No data were available for the equinoxes September 2013, March 2014, and March 2015; data for the September 2017 equinox were available but were not used because of the clearly high geomagnetic activity up to about the middle of September or so (e.g., Clilverd et al., 2018; Dimmock et al., 2019) and then another later burst (Kp = 6+/7− on September 27/28). Over the 10 available equinoctial periods (220 days in total) between 2014 and 2020, the average day-night changes in phase and amplitude were 62° and 6.2 dB, respectively.

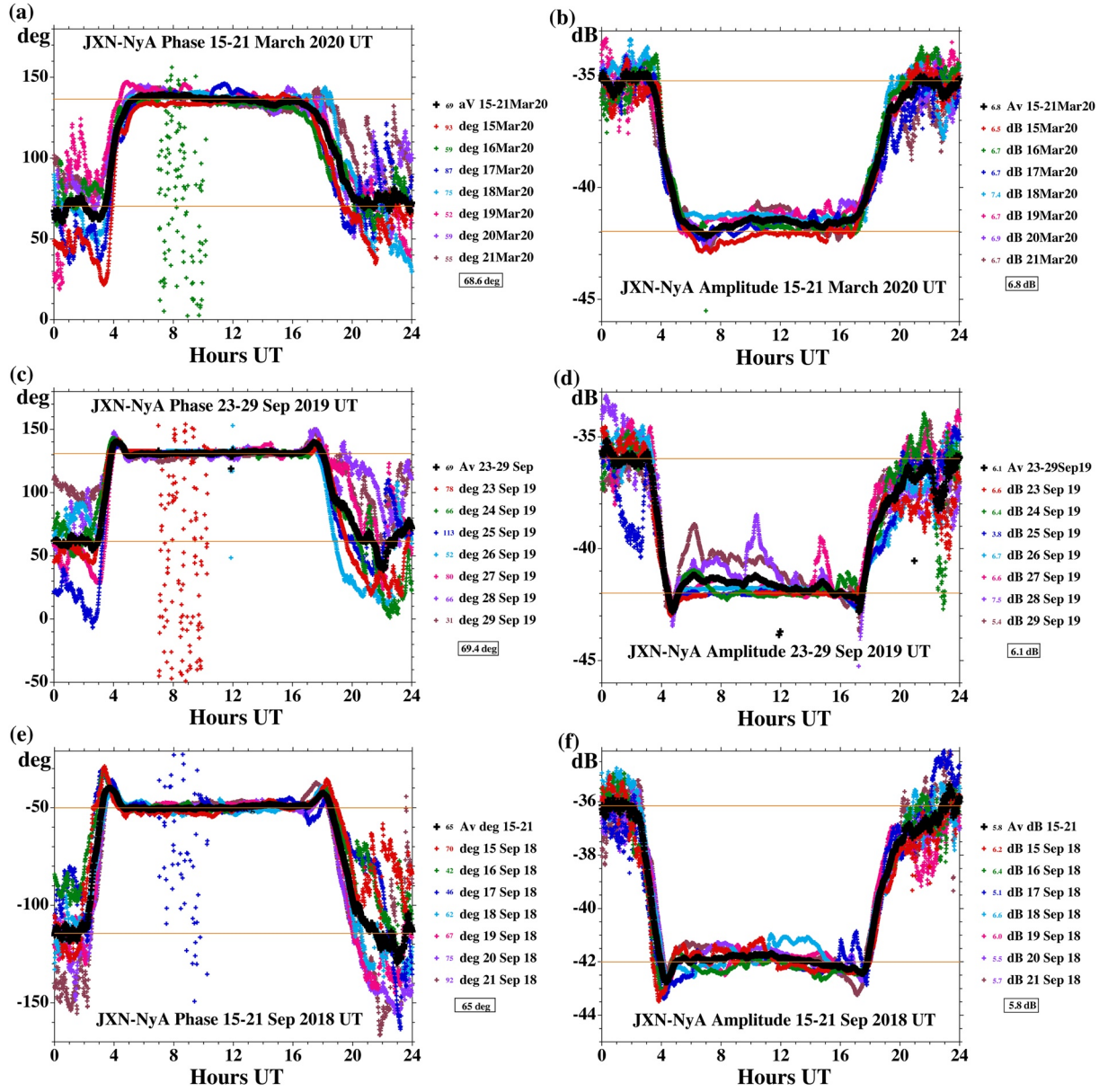

Figure 2. The observed diurnal phase and amplitude changes of JXN (16.4 kHz, ~67°N) at Ny-Ålesund (~79°N) near equinox. (a, b) March 15–21, 2020 UT. (c, d) September 23–29, 2019. (e, f) September 15–21, 2018.

2.2. Comparing with Calculations: Determining Arctic Nighttime H' and β

A slightly modified version (e.g., Thomson et al., 2018) of the US Navy code LWPC (Long Wave Propagation Capability; Ferguson & Snyder, 1990; see also Ferguson, 1998) was used to calculate the phase and amplitude of JXN (16.4 kHz) 1,334 km to the north at Ny-Ålesund, using an appropriate range of D region parameters. These calculated phases and amplitudes were then compared with the observations to look for a match and so determine which D region parameters best describe the night polar D region. As previously for the daytime Arctic D region and for the day and night D regions at lower latitudes (e.g., Thomson, 1993, 2010; Thomson & McRae, 2009; Thomson et al., 2007, 2011a, 2011b, 2012, 2014, 2017, 2018), the D region was modeled with the Wait height and sharpness parameters H' and β (Wait & Spies, 1964). Figure 3a shows the calculated phases at Ny-Ålesund for a range of H' and β, as colored lines with plot symbols described in the legend to the right. The calculated phases plotted on the left-hand side in the graph panel (heights, H', below ~74 km) are most appropriate for daytime while those on the right-hand side (heights, H', above

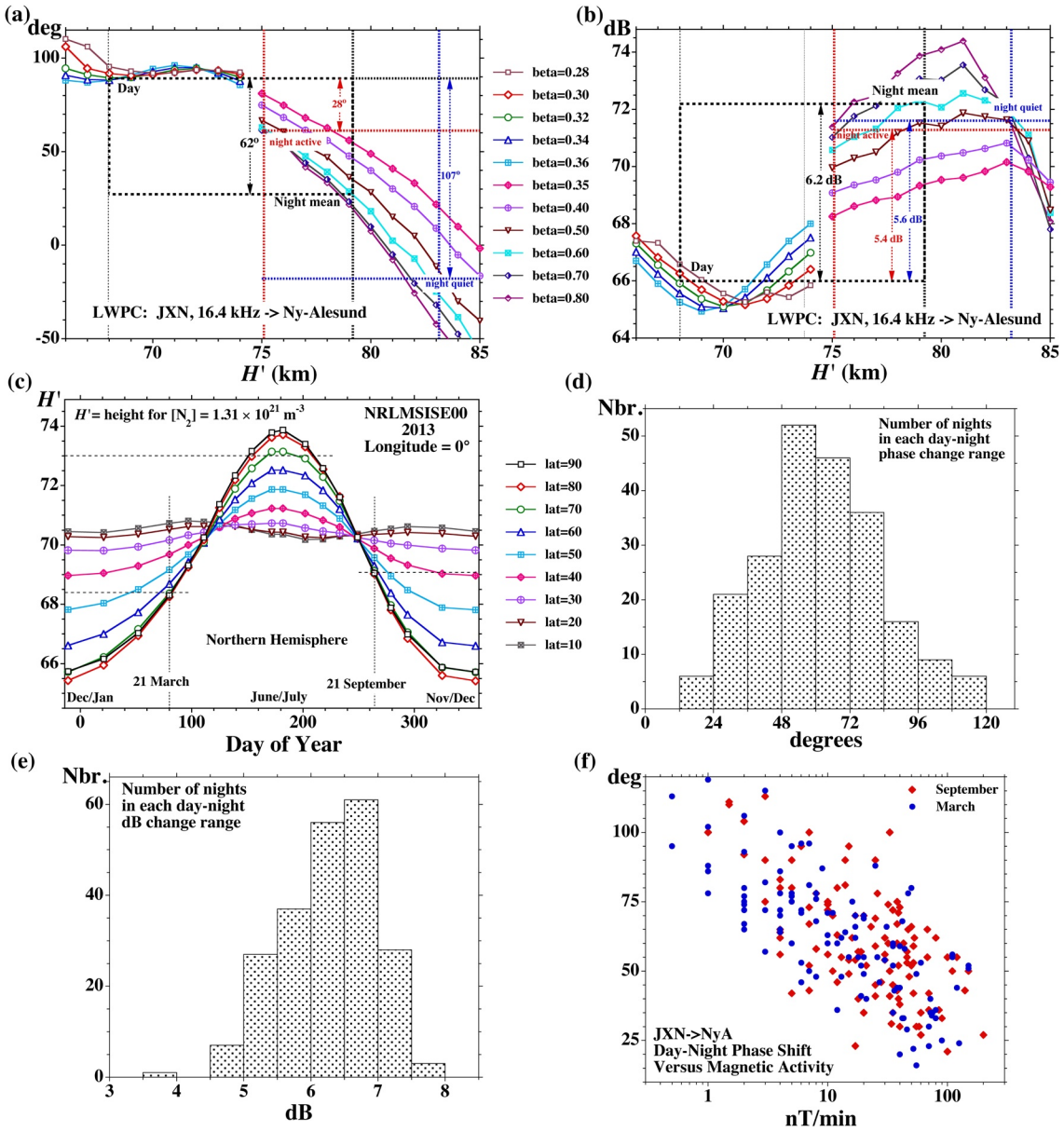

Figure 3. Results from the JXN to Ny-Ålesund path at equinox. (a, b) LWPC calculations of (a) the phases and (b) the amplitudes of JXN at Ny-Ålesund for a range of values of H' and β compared with the observed day-night phase and amplitude changes: black dashed rectangles with numbers show the mean changes, while the blue and red dotted lines with numbers show these changes for the quietest and most active 10% of nights respectively. (c) The seasonal changes in the values of H' as functions of latitude calculated from the neutral atmosphere model NRLMSISE00. (d, e) Histograms of the occurrence rates of observed day-night changes in (d) phase and (e) amplitude for equinoxes in the period 2014–2020. (f) Observed day-night phase changes as a function of magnetic activity measured in dB/dt (see text) at the nearby magnetic observatory at Abisko in Sweden.

~75 km) are more appropriate for nighttime. Similarly Figure 3b shows the calculated amplitudes for the same values of H' and β.

Thomson et al. (2018) found that the daytime summer D region in the Arctic in early June (at least in 2013) was best modeled with $H' = 73.7$ km and $\beta = 0.32$ km^{-1}. Before plotting this point in Figures 3a and 3b, allowance needs to be made for the D region altitude in summer being higher than at equinox in March or September because the neutral air temperature between these heights and the Earth's surface is mainly higher in the polar summer than at polar equinox. In Figure 3c, the NRLMSISE-00 neutral atmosphere model (https://ccmc.gsfc.nasa.gov/modelweb/models/nrlmsise00.php) has been used to calculate the seasonal height changes for the level where $[N_2] = 1.31 \times 10^{21}$ m^{-3}; this value is slightly arbitrary but is chosen to be

the same as was used to fit measured H' values in a similar but lower latitude plot in Thomson et al. (2011b). As can be seen here, Figure 3c predicts $H' = 68.4$ km in the Arctic at the March equinox and $H' = 69.1$ km at the September equinox which would average at 68.75 km. However, for early June, the plot gives H' as ∼73.0 km whereas the 2013 measurements of Thomson et al. (2018) found $H' = 73.7 \pm 0.7$ km, so that taking H' as ∼69.0 km might appear to be a better compromise estimate for average daytime Arctic equinox. However, increased auroral and geomagnetic activity near the equinoxes (e.g., Lockwood et al., 2020) as compared with (say) the June solstice, means that the equinoctial value of H' is likely to be a little lower than the ∼69.0 km deduced above due to increased electron precipitation which is likely a significant determinant of daytime H' in the polar regions (Thomson et al., 2018).

In Figures 3a and 3b, the above observed 220-days-average equinoctial day-night changes of 62° in phase and 6.2 dB in amplitude are depicted as the heights of the superposed black dashed rectangles in each figure. Although the heights of these rectangles are well-determined from the observations, the exact placement of the lower left (or "day") corner of the amplitude rectangle in Figure 3b requires some additional considerations. This "day" corner should likely be near the $\beta = 0.32$ km^{-1} contour as observed for June 2013 (as noted above). It could be at $\beta = 0.32$ km^{-1} and $H' = 69.0$ km (as deduced above, i.e., at amplitude 65.4 dB on the ordinate) but this would be making virtually no allowance for extra geomagnetic activity and precipitation at equinox compared with (June) solstice. Hence, the "day" corner could well be lower at, say, $H' = 67.0$ km and $\beta = 0.32$ km^{-1} which would give a higher daytime calculated amplitude of ∼66.7 dB, nearly the same as for the June solstice values of $H' = 73.7$ km and $\beta = 0.32$ km^{-1}. However, this would then result in rather high nighttime values of β; the mean nighttime β would be 0.7–0.8 km^{-1} which is possible but, as half the day-night amplitude changes are greater than 6.2 dB, and many (see Figure 3e) are ∼1 dB higher, i.e., around 7.2 dB, the resulting inferred values of polar nighttime β would, in Figure 3b, be much higher than the 0.6–0.7 km^{-1} measured at night at low and middle latitudes (Thomson & McRae, 2009; Thomson et al., 2007). This seems unlikely. Hence, a compromise position for the "day" corner of the amplitude rectangle in Figure 3b was chosen, as shown, at $\beta = 0.32$ km^{-1} and $H' = 68.0$ km (i.e., at an amplitude of 66.0 dB). This means the "day" or upper left corner of the phase rectangle in Figure 3a must also be taken at 68.0 km. Then, in both Figures 3a and 3b, the rectangles must be extended to the right into the nighttime contours until they both have the same nighttime values of and H' and β. This can thus be seen to give $H' = 79.2$ km and $\beta = 0.6$ km^{-1} for the mean night polar equinoctial ionosphere. Note that, while the exact placement of the dashed rectangle has small but noticeable effects on the nighttime amplitudes and values of β in Figure 3b, the corresponding effects on the phases and heights, H', in Figure 3a are near negligible.

2.3. Variations in Day-Night Phase and Amplitude Shifts, and in H' and β

As was seen in the observational plots of the JXN to Ny-Ålesund phases and amplitudes in Figure 2, there are significant geophysical variations from day-to-day in the day-night changes in both phase and amplitude about their mean values. The distributions of these variations in day-night changes in phase and amplitude are shown in the histograms in Figures 3d and 3e, respectively. To avoid the difficulty of deciding exactly when the night begins, and for systematic convenience, the night phases and amplitudes were generally measured between 0 UT and the first signs, in the plots, of dawn starting to break, normally between 1 and 3 UT, i.e., typically averaged over a period of ∼2 h after midnight. As can be seen from the plots in Figure 2, the daytime phases and amplitudes were not typically very time dependent (i.e., little solar control as noted above) and so were generally taken as an average of an hour or two either side of midday (∼11 UT) but, particularly in the case of amplitude, excluding any disturbances, especially like those in Figure 2d.

The range of these variations in the (equinoctial) night ionosphere is depicted in a different way in Figure 3a where the average phase shift for the 22 (10%) of the 220 equinoctial nights which had the largest day-night phase shifts (which corresponded approximately to the quietest nights) is shown as the dotted blue horizontal line 107° below the day phase (as opposed to the 62° for the mean night). Correspondingly, in Figure 3b the blue dotted line shows the mean amplitude (5.6 dB above the day amplitude) for these same 22 quiet equinoctial nights (i.e., those with the greatest phase shifts). As can be seen in Figures 3a and 3b, the corresponding height and sharpness for these 22 quiet nights are $H' = 83.2$ km and $\beta = 0.52$ km^{-1}. Similarly the average phase shift for the 22 (10%) of the 220 equinoctial nights here with the smallest day-night phase shifts (corresponding approximately to the most active of the 220 nights) was 28° as illustrated by the

red dotted lines in Figure 3a and correspondingly as 5.4 dB average in Figure 3b. From these two figures, it can be seen that the corresponding height and sharpness for these 22 active nights are $H' = 75.1$ km and $\beta \sim 0.8$ km^{-1}. While this indicates that low values of H' correspond to higher magnetic activity and accompanying higher precipitation, this value of $H' \sim 75$ km does not represent any sort of high activity limit because the 220 days included in the data set here intentionally excluded a small number of high activity days, specifically those near the September equinox of 2017.

On the other hand, the $H' \sim 83$ km for the 10% of least active nights is a more meaningful (upper) limit because no nights were excluded because of low activity. It is interesting to now compare this upper limit of $H' \sim 83$ km for the least active polar nights here with the $H' = 85.1 \pm 0.4$ km found by Thomson et al. (2007) for a variety of low and middle latitudes on quiet nights where precipitation did not appear to be making significant contributions to production. Calculations using NRLMSISE-00, similar to those shown in Figure 3c but for a height of 85.1 km at night for the paths used by Thomson et al. (2007), give, on average, $[N_2] \approx 1.30 \times 10^{20}$ m^{-3} (range ~1.1–1.4 $\times 10^{20}$ m^{-3}). NRLMSISE-00 also shows that, for the JXN to Ny-Ålesund path at the March/September equinoxes, this value of $[N_2] \approx 1.30 \times 10^{20}$ m^{-3} occurs at the just slightly lower average height of ~84.25 km. It can thus be seen that at times of lowest activity, and so lowest precipitation fluxes, polar H' and likely the dominant polar production sources too are tending close to the situation at nonpolar latitudes—i.e., driven by Lyman-α from the geocorona and galactic cosmic rays (e.g., Thomson et al., 2007).

To further investigate the role of magnetic activity and accompanying precipitation in ionizing the lower polar D region, at least for the JXN to Ny-Ålesund path, magnetometer records were examined from the Swedish site at Abisko (68.36°N, 18.82°E), ~200 km from this path and in the vicinity of the auroral electrojet. In Figure 3f, each day-night phase shift in degrees (representative of the D-region height at night as seen in Figures 3a and 3b) is plotted against the corresponding peak range of dB_x/dt in nT/min, on a log axis scale (representing the auroral electrojet activity levels and so the likely precipitation fluxes) for the 220 equinoctial nights here, in the same nighttime interval, 0 UT to dawn (~2–3 UT) as used in Section 2.1 for averaging each night's phase in degrees. Values of dB_x/dt at Abisko were obtained from INTERMAGNET (https://www.intermagnet.org/data-donnee/dataplot-eng.php?type=dbdt_xyz) which plots $\Delta B_x/\Delta t$ as dB_x/dt using 1-min Bx data, i.e., $\Delta t = 1$ min, so that there are 60 values per hour of $dB_x/dt = \Delta B_x/\Delta t$ in their plots. The peak range values of dB_x/dt plotted here in Figure 3f are the differences between the most positive and most negative values of dB_x/dt appearing in each of the relevant 2–3-h time intervals. While there is a fair amount of scatter in Figure 3f, there is nonetheless a clear correlation with higher activity (higher dB_x/dt) associated with smaller day-night phase shifts, corresponding to the lower edge of the night D region forming at lower altitudes when there are higher levels of precipitation, and at higher altitudes for lower levels of precipitation.

Figure 4 shows examples of JXN to Ny-Ålesund observations in 2014 and 2015, thus near to solar maximum. For many, but not all of the recordings, in the period 2014–2016, e.g., those for 2014 shown here, JXN was on-air for only 1 or 2 h in every 4 h. The receiver phase is modulo 90° (Thomson, 2017), and although rather apparent in these on/off sequences, is fortunately fairly readily allowed for, even in these on/off sequences, for JXN here on 16.4 kHz. In Figure 4e, the day-night phase shift vs. year, and so solar cycle, shows a tendency for smaller day-night phase shifts toward solar maximum likely caused by slightly more nighttime precipitation then, resulting in a slight lowering of the night D region.

3. NRK to Ny-Ålesund and JXN to Iceland

3.1. NRK (Iceland) to Ny-Ålesund

Signals from VLF transmitter, NRK (63.85°N, 22.47°W) near Grindavik, Iceland, on 37.5 kHz modulated with 200-baud MSK, are also received on the loop antenna system at Ny-Ålesund, 2,014 km to the north-northeast of the transmitter. The path, which is again mainly over the sea, is shown in Figure 1a. Examples of the resulting observed diurnal phase and amplitude variations, from the fairly typical equinoctial period September 15–21, 2019, are shown in Figures 5a and 5b, respectively. Calculated phases and amplitudes for the path, using LWPC, are shown in Figures 5c and 5d, respectively, where the range of values of H' and β is similar to those used for the JXN to Ny-Ålesund path (in Figures 3a and 3b).

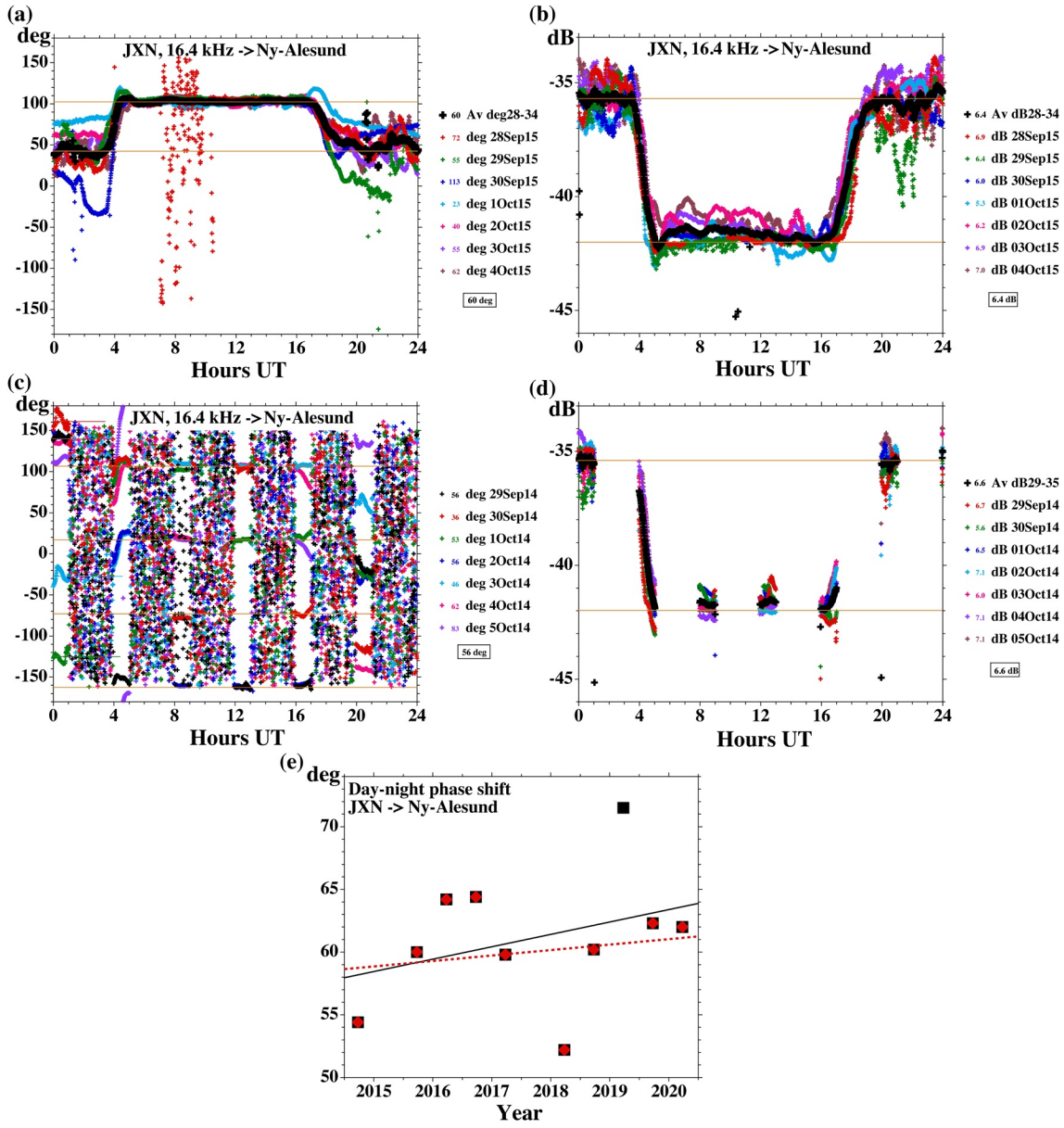

Figure 4. Similar to Figure 2 but extending back to 2014 (near solar maximum). (a, b) September 28 to October 4, 2015. (c, d) September 29 to October 5, 2014. Note JXN on-air for only 1 h in 4. (e) Mean day-night phase shift vs. year from solar maximum (~2014) to solar minimum (2019–2020) showing only marginal change. The black line is best fit to all 10 (black) points. The red line is best fit to the nine red points (i.e., when the point for March 2019 is omitted to give an indication of the marginality of the slope).

In Figure 5a, it can be seen that the average observed day-night phase shift for NRK to Ny-Ålesund is 210° which, mainly due to the much higher transmitter frequency of 37.5 kHz and the somewhat longer path, is much larger than the average 62° for the JXN to Ny-Ålesund path. This day-night shift of 210° is then used in the calculated phase plots of Figure 5c as the height, in degrees, of a dashed phase rectangle in a very similar way to that in Figure 3a for JXN to Ny-Ålesund. The upper left (i.e., the "day") corner of this dashed rectangle is at $H' = 68.0$ km and $\beta = 0.32$ km^{-1} to match with Figure 3a above. As can be seen, when the dashed rectangle was extended to the right into the night parameter region to meet the $\beta = 0.6$ km^{-1} contour (as found above for the similar Arctic path, JXN to Ny-Ålesund), the height, H', can be seen to be ~79.3 km, essentially the same as was found for the JXN to Ny-Ålesund path. This agreement thus provides some further support (in addition to that already given in Section 2.2) for taking 68.0 km as the daytime value of H' here in the Arctic at equinox. A cursory examination of several other NRK to Ny-Ålesund equinoctial

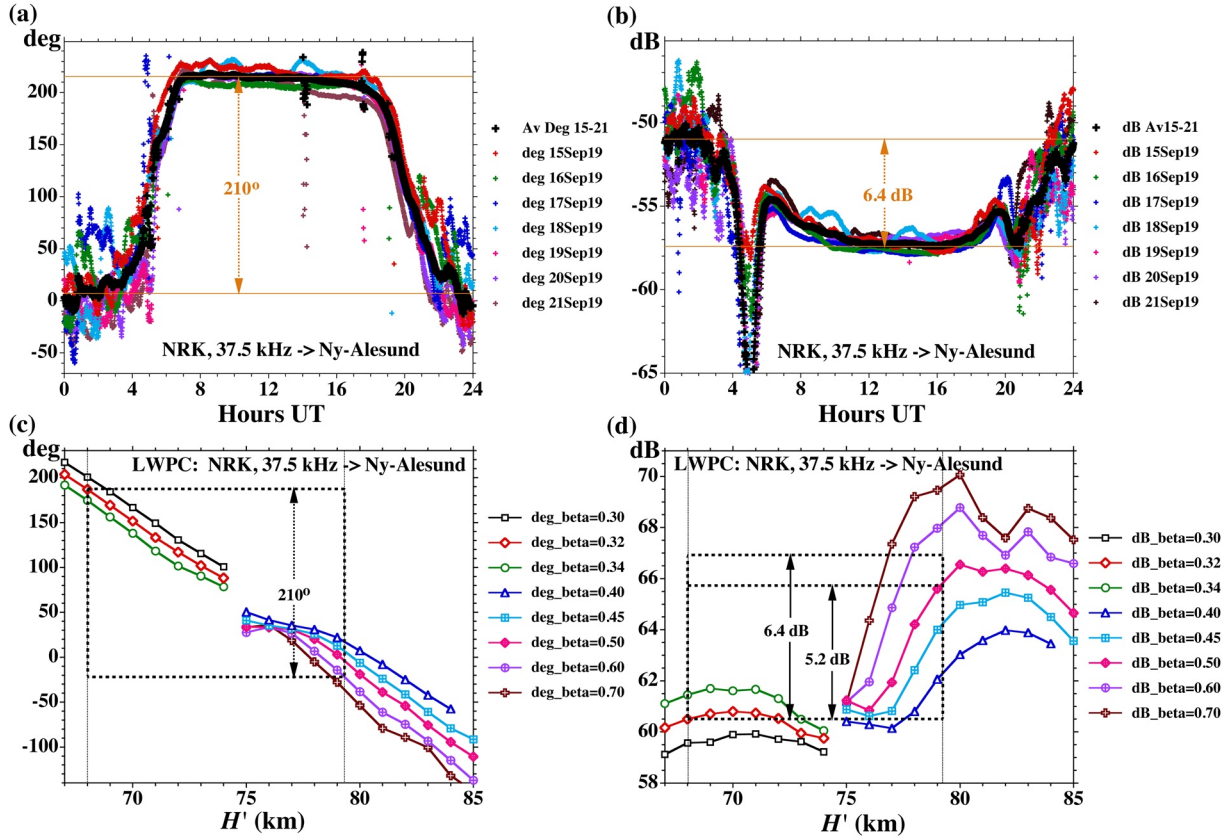

Figure 5. Similar to Figures 2 and 3a, 3b but for the path NRK to Ny-Ålesund.

periods (March and September) between 2014 and 2020 was fairly supportive of 210° being close to the average day-night phase shift. However, even though, unlike JXN, NRK was on fairly continuously (i.e., did not have periods when it was on for only one hour in four or one hour in two, etc.), it was nonetheless not always easy to identify, or rule out, 90° phase jumps on NRK (on 37.5 kHz as opposed to JXN on 16.4 kHz) during dawn or dusk. This uncertainty meant that a formal averaging analysis of the equinoctial, NRK to Ny-Ålesund observations was not likely to improve the average day-night phase shift estimate and so was not implemented.

The observed day-night amplitude change in Figure 5b is ~6.4 dB; when this is used in the calculated amplitude plots in Figure 5d with the lower left, or "day" corner, of the dashed amplitude rectangle at $H' = 68.0$ km and $\beta = 0.32$ km^{-1}, the night value of $H' = 79.3$ km (from Figure 5c) corresponds to $\beta = 0.55$ km^{-1}, rather than 0.6 km^{-1}. If this fairly small difference were the only amplitude related uncertainty for the 37.5-kHz, NRK to Ny-Ålesund path, it might not be of any real significance. However, there were some additional issues. For the three March equinoctial periods examined (2017, 2019, and 2020) the daytime amplitude was very variable and typically much lower (5–15 dB or more) than for the September equinoxes, giving large and clearly inappropriate day-night shifts. By late April the daytime amplitudes had greatly stabilized and if these daytime amplitudes were used with the March night amplitudes (there being very little night, if any, by late April), day-night amplitude shifts of ~7–8 dB were found, which would fit with $H' = 79.3$ km and $\beta = 0.6$ km^{-1} in Figure 5d (and thus would agree with the results from JXN to Ny-Ålesund in Figures 3a and 3b). For the September equinoxes, the daytime NRK to Ny-Ålesund amplitudes were generally well behaved but the average day-night shift appeared to be ~5.2 dB, i.e., lower than the 6.4 dB for September 15–21, 2019 in Figure 5b. The reasons for these amplitude issues are not known. They may possibly relate to the rather high frequency of 37.5 kHz being sensitive to some amplitude peculiarities in the Arctic ionosphere.

Nonetheless, as indicated above, if β is taken as 0.6 km^{-1}, from the 16.4 kHz JXN to Ny-Ålesund measurements, then the average 210° day-night phase shift for the September equinoxes observed for the NRK to

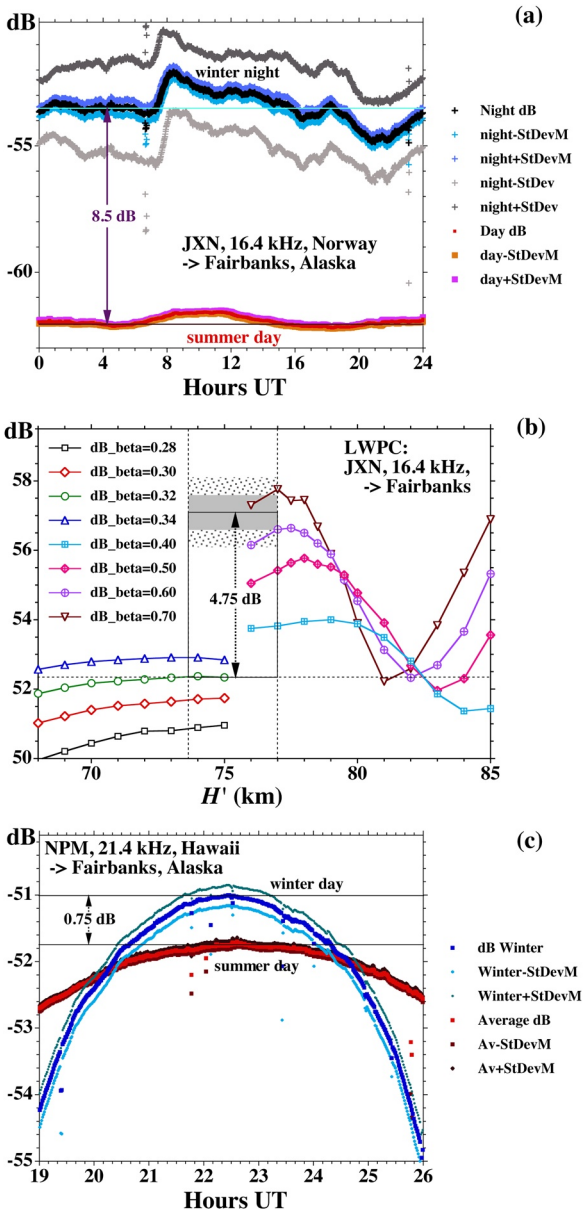

Figure 6. Amplitudes (only) for the long (5,300 km) JXN to Fairbanks path over the Arctic Ocean. (a) The recorded summer day (red) and winter night (black) mean amplitudes showing the day-night difference (8.5 dB). (b) The LWPC calculated amplitudes of JXN at Fairbanks for appropriate ranges of H' and β (day below ~75 km and night above 75 km). (c) Mean amplitudes for NPM during winter day (blue) and summer day (red) recorded at Fairbanks to check the seasonal antenna change. See text for details. LWPC, Long Wave Propagation Capability.

Ny-Ålesund path agrees very well, in Figure 5c, with the $H' = 79.2$ km and $\beta = 0.6$ km^{-1} found from the JXN to Ny-Ålesund path in Figures 3a and 3b, based on the observations at all available equinoxes.

3.2. JXN (Norway) to Reykjavik (Iceland)

As indicated in the Supporting Information, observations from the VLF path JXN to Reykjavik together with the corresponding LWPC calculations also provide some support for the night polar values of $H' = 79$ km and $\beta = 0.6$ km^{-1} determined above.

4. JXN (Norway) to Fairbanks (Alaska)

The 16.4-kHz signals from the Norwegian transmitter JXN (66.98°N, 13.87°E) have also been monitored at Fairbanks (64.8737°N, 147.8605°W), using a VLF receiver running the UltraMSK software, since November 2018. The 5,302-km path is shown in Figure 1b where it can be seen to be largely over the Arctic Ocean, passing fairly near Ny-Ålesund and the North Pole, with only a small proportion (~11%) being over land (in northern Alaska). The path covers about 162° of longitude or ~10.8 h of local time so the only times when it is completely in darkness are in the winter, and the only times when it is completely in daylight are in the summer. This meant that it was not practicable to determine the phase difference between day and night because the phase jumps or instabilities of the transmitter (in particular) and the receiver could not be readily tracked and compensated for over the ~6 months between all-day and all-night. However, the amplitude of the transmitter (i.e., the power radiated) does not suffer this difficulty because it is normally very stable and, on the rare occasions when JXN operated on reduced power, this could be checked and detected on the relatively nearby receivers at Ny-Ålesund, Reykjavik, or Eskdalemuir (Scotland). Phase jump errors accumulate but amplitude changes do not; hence use of amplitude changes only was appropriate here.

Figure 6a shows the observed amplitudes of JXN at Fairbanks vs. hours UT. The red curve near the bottom of the plot (at ~−62.0 dB) shows the average amplitude for summer daytime for the period June 2–28, 2019 UT while the black line in the upper part of the plot shows the winter night average amplitude (at ~−53.5 dB) for ~43 (39–45) "days" from the winter periods November 22 to December 11, 2018, January 14 to February 3, 2019, and November 22 to December 4, 2019. Basically, this included all available winter "days" (i.e., nights) when JXN was on-air, and the receiver was operating correctly, except for December 5–9, 2019 after JXN went off-air for an hour or so and then came back on-air on reduced power. No valid data were available for January 2020 because of a receiver fault. The data are plotted at 1-min resolution. For each minute, the standard deviation was calculated for the ~43 winter nights; the two gray curves are at one standard deviation on each side of the black average winter night curve to give an indication of the amount of (geophysical) scatter from night to night. For each minute, the standard deviations were also divided by the square root of the number of nights (~43) to give the standard deviation of the mean; the two bluish lines immediately on either side of the black average line are at one standard deviation of the mean from the average line, thus displaying the small measure of uncertainty in dB of the black average line. Similarly, for the summer day curve, the red/orange lines on either side of the average line are at one

standard deviation of the mean from it. While more summer days were available (e.g., in July) the ∼21 used in the average are clearly sufficient to get a good low statistical error.

In Figure 6a, midnight and midday at the midpoint of the path are at ∼4 and ∼16 UT in winter and summer, respectively. As can be seen, the recording is showing 8.5 dB difference in amplitude between midday and midnight. Figure 6b shows the LWPC amplitude calculations for this JXN-Fairbanks path for appropriate values of H' and β. The dotted vertical line at $H' = 73.7$ km together with the dotted horizontal line at $\beta = 0.32$ km^{-1} show the summer day values previously measured from the JXN to Nome, Alaska, path (Thomson et al., 2018) which can be expected to be very similar to the JXN-Fairbanks path. It is immediately apparent that the recorded observed value of 8.5 dB, between summer day and winter night amplitudes, is much too large. The reason for this is very likely due to the gain of the receiving system at Fairbanks being lower in summer than in winter. This occurs because, at Fairbanks, unlike at most other AARDDVARK receiving sites, the receiving antenna is a vertical dipole (measuring the vertical electric field, E_z) rather than a loop (measuring the magnetic field, H_y). The Fairbanks antenna is also in a clearing in a forest of tall trees and its gain has been observed to be significantly sensitive to rain with, e.g., both the NPM and JXN amplitudes dropping markedly during rainy days such as June 1, 2019. While such rain effects are not a common occurrence, they are nonetheless fairly unequivocal; examples can be seen in the Supporting Information.

The extent of the seasonal change in gain can be found from the recorded observations of NPM, Hawaii, at Fairbanks shown in Figure 6c, when compared with LWPC calculations for this all-sea, mainly low and midlatitude path. In Figure 6c, the summer day amplitudes averaged are from June 2 to 28, 2019 (as for the summer day amplitudes for JXN in Figure 6a), while the winter day amplitudes averaged are those available from December 2018, January 3–6, 2019 and late November 2019, being about 31 days in total. As can be seen, the winter day average amplitude was recorded as 0.75 dB higher than the midday summer amplitude. For the LWPC calculations, appropriate solar zenith angle dependent values of H' and β were determined based on the season (summer or winter) and the varying latitudes along the path. These midday values of H' and β were estimated along both the summer and the winter paths from the observational results of Thomson et al. (2011a, 2011b, 2014, 2017, 2018), McRae and Thomson (2000), and Thomson (1993). LWPC was thus found to predict the midday amplitude, in dB > 1 μV/m, of NPM at Fairbanks in summer as 60.8 (corresponding to $H' = 70.2$ km and $\beta = 0.45$ km^{-1} averaged along the path) and in winter as 57.8 (corresponding to $H' = 74.3$ km and $\beta = 0.32$ km^{-1} averaged along the path). Thus the receiver (antenna) gain at Fairbanks was greater in winter than in summer by 60.8–57.8 + 0.75 = 3.75 dB. Hence, the 8.5 dB by which JXN's winter night amplitude appears greater than its summer day amplitude in Figure 6a needs to be reduced by this 3.75 dB to give the true night-day measured amplitude difference as 8.5–3.75 = 4.75 dB which is thus shown appropriately in Figure 6b as an increment from the summer day value of 52.3 dB (at $H' = 73.7$ km and $\beta = 0.32$ km^{-1}).

While the amplitude only observations for JXN-Fairbanks cannot fully define the height, H', they do provide some constraints: Figure 6b does indicate that night values of H' in the range ∼79–84 km are rather unlikely. However, the night height $H' = 79.2$ km determined from the JXN to Ny-Ålesund path at equinox in Section 2.2 can be used after adjusting it to winter. At a height of ∼79 km, NRLMSISE-00 finds $[N_2] \approx 3.0 \times 10^{20}$ m^{-3} at equinox but in midwinter this value of $[N_2]$ occurs at a height of ∼76 km, nearly 3 km lower. However, as mentioned above, because geomagnetic activity and precipitation are likely to be lower on average near winter solstice compared with equinox, a better estimate for average H' in the Arctic winter night is likely ∼77 km which is shown as dotted vertical line in Figure 6b. The likely uncertainty in the 4.75 dB night-day amplitude estimated in the last paragraph is probably dominated by the uncertainty in the winter propagation calculation because summer day is generally more predictable and most of the observations in the references cited relate to summer or equinox conditions. This also means it is not entirely straightforward to estimate the uncertainty in the winter day calculations. However, it seems the uncertainty is not likely to be <±0.5 dB but could be up to ∼±1 dB. These uncertainties are shown as shaded and dotted in Figure 6b where it can also be seen that the night amplitude on the long JXN-Fairbanks path is consistent with $\beta = 0.6$ km^{-1} and $H' = 77$ km in winter and so (as discussed above) with $\beta = 0.6$ km^{-1} and $H' = 79.2$ km from the JXN to Ny-Ålesund path at equinox.

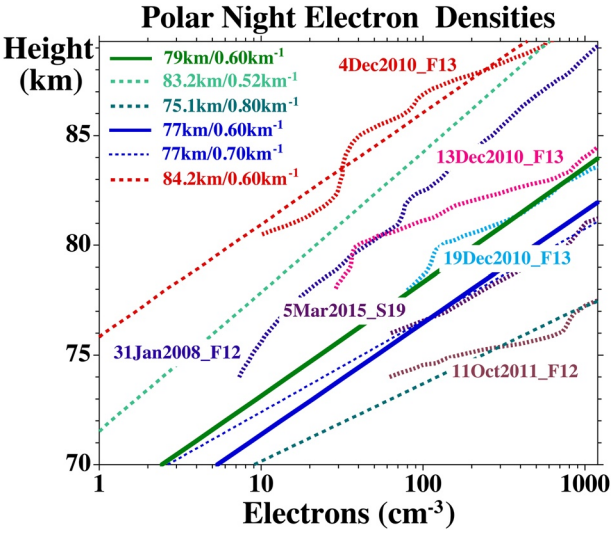

Figure 7. Observed polar night electron number densities. The six straight lines, blue for winter and green for equinox, are the results from VLF radio propagation here, with their H' and β values given in the legend at top left. The solid lines are the averages for winter (blue) and equinox (green), respectively. The dashed green lines show the 10-percentile and 90-percentile equinoctial limits from Figures 3a and 3b here. The dashed blue line is explained in the text. For comparison with the VLF results, the six curved dotted lines are each from a single rocket profile (with date as shown) from Friedrich et al. (2012) (F12), Friedrich et al. (2013) (F13), and Strelnikov et al. (2019) (S19). The straight red dashed line is a (H', β) best fit to the rocket profile of December 4, 2010. VLF, very low frequency.

5. Comparisons with Others and Electron Number Densities

5.1. H' and β Comparisons, in Particular with the US Navy

Forty year ago, Ferguson (1980) reported on the night D region parameters for the US Navy using VLF radio amplitude observations on aircraft flight paths. Two of these paths were in the Arctic or had a significant part in the Arctic: two flights from Sentinel, Arizona (32.8°N, 10 frequencies) ~northwards to Thule (78.5°N, Greenland) one each on February 5 and 6, 1974, and a flight from JHZ (16.4 kHz, 66.4°N, ~70 km south of current JXN) northward and over the North Pole (toward Hawaii) on February 6, 1977. For the polar part of the Sentinel-Thule path, the best fit was reported as $H' = 77$ km with $\beta = 0.8$ km^{-1} (14–28 kHz); for the path from JHZ over the North Pole the best fit was reported as $H' = 80$ km with $\beta = 0.5$ km^{-1} (Table 4 in Ferguson, 1980). The LWPC's "polar night model" (not used here) has $H' = 80.5$ km with $\beta = 0.33$ km^{-1} programmed in. The CCIR (1990, now ITU) recommended, for polar latitudes, $H' = 76$ km with the same frequency dependent β as recommended by Ferguson (1980), $\beta = 0.035f - 0.025$ km^{-1} where f is the frequency in kHz (giving $\beta = 0.55$ km^{-1} at 16.4 kHz). The concept of a frequency dependent β did not appear to have a physical justification and does not seem to have been adopted elsewhere.

5.2. Electron Number Densities

As discussed by Thomson et al. (2018), Wait and Spies (1964) showed it was convenient to characterize the ionized D region of the ionosphere by using the parameter $\omega_r = \omega_o{}^2/\nu$ where ν is the electron-neutral collision frequency and ω_o is the angular (electron) plasma frequency; hence, $\omega_r \approx 3{,}183N_e/\nu$ where N_e is the electron number density (since $e^2/\varepsilon_o m_e \approx 3{,}183$). Wait defined the height at which $\omega_r = 2.5 \times 10^5$ rad/s as H', and ω_r was taken to vary with height, h, as $\omega_r = 2.5 \times 10^5 \exp(h - H')\beta$, thus defining β as a (near) constant with height, but varying with latitude, time of day, and solar cycle. This parameterization has been widely and successfully used (e.g., Thomson et al., 2018). Hence, having determined values of H' and β from propagation measurements and modeling, as in Sections 2–4, here, ω_r can be found over a range of heights, h, from $\omega_r = 2.5 \times 10^5 \exp(h - H')\beta$ thus allowing N_e to be determined from $\omega_r \approx 3{,}183N_e/\nu$ above, once the effective collision frequency, ν, has been determined. From Figure 2 of Deeks (1966), $\nu \approx 2.4\nu_m$ for the heights of 75–85 km here, where ν_m is the monoenergetic collision frequency given by $\nu_m = Kp$ where p is the pressure at height, h, and $K = 6.4 \times 10^5$, in SI units (Friedrich & Torkar, 1983). The pressure can be found from $p = nkT$ where k is Boltzmann's constant, while n, the neutral number density, and T, the neutral temperature, can be found from the NRLMSISE-00 atmospheric model.

When this was done (more detail can be found in Thomson et al. (2018)), electron number densities vs. height were determined and are shown as the straight lines plotted in Figure 7 where the green lines are appropriate for equinoctial polar night and the blue lines are for winter polar night. The solid lines are the mean values, from the VLF observations reported here, for equinox (green) and winter (blue) while the dashed green lines are for the equinoctial upper and lower 10-percentile values determined in Section 2.2 and illustrated in Figures 3a and 3b. The dated dotted curves are from the rocket MF/HF radio wave propagation measurements of Friedrich et al. (2012, 2013) and Strelnikov et al. (2019) at ~69°N above Andøya, Norway. The (thin) blue dashed line was calculated for $H' = 77$ km and $\beta = 0.7$ km^{-1} for comparison with the slope of the $H' = 77$ km and $\beta = 0.6$ km^{-1} mean winter solid blue line and the slopes of the rocket observations. With the possible exception of the red rocket curve for December 4, 2010 near the top of Figure 7 (see below), the electron number density rocket-measured curves clearly have similar slopes and height ranges to the VLF-measured lines. Similarly, Singer et al. (2011) using a vertically directed MF (3.19 MHz) radar also from Andøya near 69°N, found similar profiles; in particular, those from December 4, 2004 and

January 2, 2005 (at solar zenith angles of 103° and 129°, respectively) track essentially between, and roughly parallel to, the solid green and blue lines in Figure 7 (though not shown there to avoid clutter).

The red rocket-measured profile for December 4, 2010 (mentioned above) at the top of Figure 7 is described by Friedrich et al. (2012) as being the lowest (electron density at each height) ever measured at auroral latitudes. Indeed it occurred during very quiet conditions: apart from a very brief spike of ~2 nT/min on B_y all the dB/dt values were below 1 nT/min, and the 3-hourly values of Kp, for at least the measurement time and the preceding 36 h, were all 0 or 0+ ($ap = 0$ or 2) apart from one at 1− ($ap = 3$). The red dashed straight line with $H' = 84.2$ km and $\beta = 0.6$ km^{-1}, shown near the top of Figure 7, is an approximate fit to this December 4, 2010 rocket profile. As in Section 2.3 above, this can also be compared with the $H' = 85.1 \pm 0.4$ km and $\beta = 0.63 \pm 0.04$ km^{-1} found by Thomson et al. (2007) for the average quiet night midlatitude D region. As already noted in Section 2.3, at 85.1 km at midlatitude [N_2] ≈ 1.30×10^{20} m^{-3}; this corresponds to an air number density ≈ 1.65×10^{20} m^{-3} which Rapp et al. (2001) observed to occur at 69°N in January-March at a height of ~83.6 km. While the midwinter (December) value of this height would be expected to be a few tenths of a km lower (perhaps 83.2 km) than the January-March value, the 85.1 km at midlatitude is an average but the plots in Thomson et al. (2007) show that night to night fluctuations are at least ~±1 km, so that 84.2 km is fairly well within the extreme range. Thus this lowest auroral electron density profile, occurring during very quiet geomagnetic conditions, does, as might be expected, seem to be minimally influenced by energetic electron precipitation (EEP), and so is generated more like a nighttime midlatitude profile, i.e., by geocoronal Lyman-α and galactic X-rays.

Additional nighttime D-region electron density profiles measured with rockets using MF/HF radio wave propagation can be found in Friedrich and Torkar (1995, Figure 5). Of these, ~20 profiles have electron densities going down to, or nearly to, 100 cm^{-3} with the average height at which this density occurs being ~74 km; i.e., somewhat below the corresponding average height in our Figure 7, and close to our lowest green dashed line ($H' = 75.1$ km, $\beta = 0.8$ km^{-1} slightly arbitrarily defined in Section 2.3 above). However, Friedrich and Torkar (1995) do not give individual details (dates, magnetic activity) for their ~20 profiles so that it could well be that their average electron number density of ~100 cm^{-3} at 74 km is higher than that seen in our Figure 7 because they have included profiles from more active times than in our Figure 7.

Comparisons between D region modeling and measured electron densities have also been made. Siskind et al. (2018), reported that their modeled electron densities, at heights where these were relatively small, ~100 cm^{-3} (at ~60–70 km by day), tended to be smaller than the rocket wave measured electron densities but their modeled values agreed more closely with VLF-measured quiet-time electron densities.

5.3. Day-Night Changes in the Polar *D* Region

At low and middle latitudes, the D region changes very markedly between day and night, as particularly evidenced by the diurnal changes in amplitude and phase along VLF radio paths (e.g., Thomson et al., 2011b, 2017). This is principally caused by the change in the main ionizing source: direct Lyman-α from the Sun by day reducing dramatically by night to the small amount of indirect Lyman-α reradiated by the hydrogen in the Earth's geocorona. As discussed above, the principal ionizing source in the polar regions is likely energetic electron precipitation both by day and by night. However, as was clear above, particularly in Figures 2–5, even in the polar regions there are also marked changes between day and night. These are likely due to changes in the electron loss processes, in particular, in the lower D region (below 70–80 km) the attachment of free electrons to neutral molecules to form negative ions (which are much too heavy to affect most radio waves, such as VLF or HF). The initial attachment is usually to an O_2 molecule: $e^- + O_2 + M \Rightarrow O_2^- + M$, where M is another neutral molecule, typically O_2 or N_2 (enabling conservation of both energy and momentum in the reaction). The speed of the reaction is thus proportional to the square of the neutral density, resulting in the reaction being significant only in the lower part of the D region where neutral densities are higher. In the absence of sunlight, these O_2^- negative ions react with other atmospheric neutrals typically resulting in other (hydrated) negative ions, based on CO_3^- and, in particular, NO_3^-, becoming the dominant negative ions in the lower D region at night, leaving very few free electrons. When sunlight returns at dawn, the electrons are rapidly photodetached from these negative ions, resulting in electrons being plentiful in the lower D region by day but not by night (e.g., Reid, 1976, 1987; Verronen, 2006). It has also been reported that atomic oxygen reinforces this effect by day by destroying negative ions; at night

the atomic oxygen concentration in the lower D region is much lower than by day because at night there is no solar radiation to dissociate O_2 molecules (Osepian et al., 2008; see also; Barabash et al., 2012; Friedrich et al., 2011). Thus at dusk the D region changes relatively slowly from day to night because the lifetime of atomic oxygen is quite long, e.g., ~2 and ~0.3 h at heights of 80 and 75 km, respectively (Banks & Kockarts, 1973), and so the atomic oxygen continues destroying the negative ions for up to an hour or two after dark, whereas at dawn, the return of sunlight photodissociates the numerous negative ions quite rapidly, as can be seen in VLF plots such as in Figures 2 and 4.

6. Discussion, Summary, and Conclusions

In Section 2, the observed day-night phase and amplitude changes for 220 (relatively undisturbed) equinoctial nights for the Arctic Ocean path from JXN (16.4 kHz, ~67°N) to Ny-Ålesund (~79°N), in the period 2014–2020, were compared with LWPC modeling for a wide range of night D region parameters, H' and β, from a daytime base inferred from the observations of Thomson et al. (2018). It was found that the polar night D region was rather variable, particularly in height, with the mean equinoctial nighttime parameters being $H' = 79.2$ km and $\beta = 0.6$ km^{-1}—i.e., markedly lower in height, on average, than the $H' = 85.1$ km found at lower latitudes by Thomson et al. (2007). As noted in Section 2, this value of 85.1 km would be lower by only just a little, at 84.25 km, in the cooler equinoctial polar ionosphere; the markedly lower H' in the polar regions (~79 vs. ~84 km) strongly implies that there is a significant further source of ionization in the polar night D region in addition to the solar Lyman-α from the geocorona and galactic cosmic rays which dominate the night D region at lower latitudes. Further the substantial observed variations in the polar H' values from ~83.2 km for the top 10% of the 220 nights through to ~75.1 km for the lowest 10% of nights is consistent with a rather variable additional source of ionization such as electron precipitation. Also significantly supporting the additional ionization coming from precipitation is the observation (from the propagation phases here) that the night values of H' vary inversely with magnetic activity ($\log(dB_x/dt)$ at nearby Abisko (Figure 3f). Vampola and Gorney (1983) showed that average nighttime polar EEP fluxes from the S3-2 satellite generate an ionization rate (at heights including 75–85 km) more than an order of magnitude greater than that from geocorona-scattered solar Lyman-α (the principal nighttime ionization source at middle and low latitudes). Recently, van de Kamp et al. (2018) have provided refined maps of EEP fluxes, measured on the POES satellites, as functions of magnetic activity, MLT and L-value, clearly illustrating the rapid increases of EEP from $L = \sim 4$ to $L = \sim 6$ (i.e., on entry to the polar regions) and with increasing magnetic activity.

In Section 3, the mean height of the equinoctial polar night ionosphere found from the principal JXN to Ny-Ålesund path on 16.4 kHz, $H' = 79.2$ km, was found to be supported by similar observations and analysis on the two similar short European Arctic paths NRK to Ny-Ålesund on 37.5 kHz and JXN to Iceland.

In Section 4, the measurements on the much longer (5.3 Mm) Arctic path, JXN to Fairbanks, Alaska, were used to show $\beta = 0.6$–0.7 km^{-1} during winter night after comparing the observed (summer) day and (winter) night amplitudes and after allowing for the seasonal changes in the electric field receiving antenna. The night amplitude measurements were also found to be consistent with $H' = 77$ km in winter as estimated from the NRLMSISE-00 atmospheric model; although the height could not be determined fully unambiguously, the VLF amplitude observations showed that night values of H' in the range ~79–84 km were quite unlikely.

In Section 5, the values of H' and β determined here from VLF observations for the night polar D region were used to calculate and plot corresponding electron number density vs. height profiles. These plots were then compared with six similar plots from the rocket-measured, in situ, wave propagation measurements of others. While our VLF technique here is generally constrained to produce straight lines for our profiles, the ranges of heights and slopes of the rocket electron density profiles generally agreed rather well with our VLF derived electron densities. While the rocket profiles are necessarily few in number, our equinoctial results used 220 nights and our winter results used ~43 nights. While the rocket profiles were all at 69°N over the Norwegian island of Andøya, our profiles are averages, in distance (rather than time) over much (1.3–5.3 Mm) of the Arctic; however, the agreement between techniques is generally rather good. Note that both these sets of results appear likely to apply to the Antarctic too.

From our VLF measurements here, the lower edge of the night polar ionospheric *D* region has been shown to be characterized on average by $\beta = 0.6$ km^{-1}, with $H' = 79$ km near equinox and $H' = 77$ km in winter. In this region the ionization is maintained almost totally by energetic electron precipitation except in rare extremely quiet conditions.

Data Availability Statement

The raw data measurements underlying our VLF observations reported here are available at http://doi.org/10.5281/zenodo.4322270. The atmospheric data shown in Figure 3c were obtained from the NRLMSISE-00 web model at https://ccmc.gsfc.nasa.gov/modelweb/models/nrlmsise00.php. The magnetometer data from Abisko were recorded by the Geological Survey of Sweden and downloaded from INTERMAGNET at https://www.intermagnet.org/data-donnee/dataplot-eng.php?type=dbdt_xyz. *Kp* and *ap* magnetic indices came from the Helmholtz Centre Potsdam-German Research Centre for Geosciences GFZ: https://www.gfz-potsdam.de/en/kp-index/(using: http://ftp.gfz-potsdam.de/pub/home/obs/kp-ap). The references cited for the non-VLF data in Figure 7 were published under a Creative Commons CC Attribution 3.0 or 4.0 License. The weather data used in the Supporting Information came from NOAA at https://www.ncdc.noaa.gov/cdo-web/search?datasetid=GHCND.

Acknowledgments
The VLF observations analyzed here were supported by funding from the UK Research and Innovation (UKRI-NERC) through National Capability-Space Weather Observatory.

References

Banks, P. M., & Kockarts, G. (1973). *Aeronomy*. New York, NY: Academic Press.

Barabash, V., Osepian, A., Dalin, P., & Kirkwood, S. (2012). Electron density profiles in the quiet lower ionosphere based on the results of modeling and experimental data. *Annales Geophysicae*, *30*, 1345–1360. https://doi.org/10.5194/angeo-30-1345-2012

Clilverd, M. A., Rodger, C. J., Brundell, J. B., Dalzell, M., Martin, I., Mac Manus, D. H., et al. (2018). Long-lasting geomagnetically induced currents and harmonic distortion observed in New Zealand during the 7-8 September 2017 disturbed period. *Space Weather*, *16*, 704–717. https://doi.org/10.1029/2018SW001822

Clilverd, M. A., Rodger, C. J., Thomson, N. R., Brundell, J. B., Ulich, T., Lichtenberger, J., et al. (2009). Remote sensing space weather events: Antarctic-arctic radiation-belt (dynamic) deposition-VLF Atmospheric Research Konsortium network. *Space Weather*, *7*, S04001. https://doi.org/10.1029/2008SW000412

Comité Consultatif International des Radiocommunications. (1990). *Radio propagation and circuit performance at frequencies below about 30 kHz* (Report 895-2, 29 pp, Dusseldorf, Germany). https://www.itu.int/dms_pub/itu-r/opb/rep/R-REP-P.895-2-1990-PDF-E.pdf

Deeks, D. G. (1966). Generalised full wave theory for energy-dependent collision frequencies. *Journal of Atmospheric and Terrestrial Physics*, *28*, 839–846. https://doi.org/10.1016/S0021-9169(17)30005-3

Dimmock, A. P., Rosenqvist, L., Hall, J.-O., Viljanen, A., Yordanova, E., Honkonen, I., et al. (2019). The GIC and geomagnetic response over Fennoscandia to the 7–8 September 2017 geomagnetic storm. *Space Weather*, *17*, 989–1010. https://doi.org/10.1029/2018SW002132

Ferguson, J. A. (1980). *Ionospheric profiles for predicting nighttime VLF/LF propagation (Nav. Ocean Syst. Cent. Tech. Rep. 530)*. Springfield, VA: National Technical Information Service. http://www.dtic.mil/dtic/tr/fulltext/u2/a085399.pdf

Ferguson, J. A. (1998). *Computer programs for assessment of long-wavelength radio communications, version 2.0: User's guide and source files* (Technical Document 3030). San Diego, CA: Space and Naval Warfare Systems Center (SPAWAR). http://www.dtic.mil/dtic/tr/fulltext/u2/a350375.pdf

Ferguson, J. A. & Snyder, F. P. (1990). *Computer programs for assessment of long wavelength radio communications, version 1.0: Full FORTRAN code user's guide, Naval Ocean Systems Center Tech*. (Doc. 1773, DTIC AD-B144 839). Alexandria, VA: Def. Tech. Inf. Cent.

Friedrich, M., Pock, C., & Torkar, K. (2018). FIRI-2018, an updated empirical model of the lower ionosphere. *Journal of Geophysical Research: Space Physics*, *123*, 6737–6751. https://doi.org/10.1029/2018JA025437

Friedrich, M., Rapp, M., Blix, T., Hoppe, U.-P., Torkar, K., Robertson, S., et al. (2012). Electron loss and meteoric dust in the mesosphere. *Annales Geophysicae*, *30*, 1495–1501. https://doi.org/10.5194/angeo-30-1495-2012

Friedrich, M., Rapp, M., Plane, J. M. C., & Torkar, K. M. (2011). Bite-outs and other depletions of mesospheric electrons. *Journal of Atmospheric and Solar-Terrestrial Physics*, *73*(14–15), 2201–2211. https://doi.org/10.1016/j.jastp.2010.10.018

Friedrich, M., & Torkar, K. M. (1983). Collision frequencies in the high latitude D-region. *Journal of Atmospheric and Terrestrial Physics*, *45*(4), 267–271. https://doi.org/10.1016/S0021-9169(83)80048-8

Friedrich, M., & Torkar, K. M. (1995). Typical behaviour of the high latitude lower ionosphere. *Advances in Space Research*, *16*(1), 73–81. https://doi.org/10.1016/0273-1177(95)00102-K

Friedrich, M., & Torkar, K. M. (2001). FIRI: A semiempirical model of the lower ionosphere. *Journal of Geophysical Research*, *106*(A10), 21409–21418. https://doi.org/10.1029/2001JA900070

Friedrich, M., Torkar, K. M., Hoppe, U.-P., Bekkeng, T.-A., Barjatya, A., & Rapp, M. (2013). Multi-instrument comparisons of D-region plasma measurements. *Annales Geophysicae*, *31*, 135–144. https://doi.org/10.5194/angeo-31-135-2013

Lockwood, M., Owens, M. J., Barnard, L. A., Haines, C., Scott, C. J., McWilliams, K. A., & Coxon, J. C. (2020). Semi-annual, annual and universal time variations in the magnetosphere and in geomagnetic activity: 1. Geomagnetic data. *Journal of Space Weather and Space Climate*, *10*, 1–23. https://doi.org/10.1051/swsc/2020023

McRae, W. M., & Thomson, N. R. (2000). VLF phase and amplitude: Daytime ionospheric parameters. *Journal of Atmospheric and Solar-Terrestrial Physics*, *62*(7), 609–618. https://doi.org/10.1016/S1364-6826(00)00027-4

Neal, J. J., Rodger, C. J., Clilverd, M. A., Thomson, N. R., Raita, T., & Ulich, T. (2015). Long-term determination of energetic electron precipitation into the atmosphere from AARDDVARK subionospheric VLF observations. *Journal of Geophysical Research: Space Physics*, *120*, 2194–2211. https://doi.org/10.1002/2014JA020689

Osepian, A., Tereschenko, V., Dalin, P., & Kirkwood, S. (2008). The role of atomic oxygen concentration in the ionization balance of the lower ionosphere during solar proton events. *Annales Geophysicae*, *26*, 131–143. https://doi.org/10.5194/angeo-26-131-2008

Rapp, M., Gumbel, J., & Lübken, F.-J. (2001). Absolute density measurements in the middle atmosphere. *Annales Geophysicae*, *19*, 571–580. https://doi.org/10.5194/angeo-19-571-2001

Reid, G. C. (1976). Ion chemistry in the *D* region. In D. R. Bates, & B. Bederson (Eds.), Advances in atomic and molecular physics (Vol. 12, pp. 375–413). New York, NY: Academic Press. https://doi.org/10.1016/S0065-2199(08)60047-0

Reid, G. C. (1987). Radar observations of negative-ion photodetachment at sunrise in the auroralzone mesosphere. *Planetary and Space Science*, *35*(1), 27–37. https://doi.org/10.1016/0032-0633(87)90141-3

Singer, W., Latteck, R., Friedrich, M., Wakabayashi, M., & Rapp, M. (2011). Seasonal and solar activity variability of D-region electron density at 69°N. *Journal of Atmospheric and Solar-Terrestrial Physics*, *73*(9), 925–935. https://doi.org/10.1016/j.jastp.2010.09.012

Siskind, D. E., Zawdie, K. A., Sassi, F., Drob, D. P., & Friedrich, M. (2018). An intercomparison of VLF and sounding rocket techniques for measuring the daytime *D* region ionosphere: Theoretical implications. *Journal of Geophysical Research: Space Physics*, *123*, 8688–8697. https://doi.org/10.1029/2018JA025807

Strelnikov, B., Eberhart, M., Friedrich, M., Hedin, J., Khaplanov, M., Baumgarten, G., et al. (2019). Simultaneous in situ measurements of small-scale structures in neutral, plasma, and atomic oxygen densities during the WADIS sounding rocket project. *Atmospheric Chemistry and Physics*, *19*, 11443–11460. https://doi.org/10.5194/acp-19-11443-2019

Thomson, N. R. (1993). Experimental daytime VLF ionospheric parameters. *Journal of Atmospheric and Terrestrial Physics*, *55*(2), 173–184. https://doi.org/10.1016/0021-9169(93)90122-F

Thomson, N. R. (2010). Daytime tropical D region parameters from short path VLF phase and amplitude. *Journal of Geophysical Research*, *115*, A09313. https://doi.org/10.1029/2010JA015355

Thomson, N. R., Clilverd, M. A., & McRae, W. M. (2007). Nighttime ionospheric *D* region parameters from VLF phase and amplitude. *Journal of Geophysical Research*, *112*, A07304. https://doi.org/10.1029/2007JA012271

Thomson, N. R., Clilverd, M. A., & Rodger, C. J. (2011). Daytime midlatitude *D* region parameters at solar minimum from short-path VLF phase and amplitude. *Journal of Geophysical Research*, *116*, A03310. https://doi.org/10.1029/2010JA016248

Thomson, N. R., Clilverd, M. A., & Rodger, C. J. (2014). Low-latitude ionospheric *D* region dependence on solar zenith angle. *Journal of Geophysical Research: Space Physics*, *119*, 6865–6875. https://doi.org/10.1002/2014JA020299

Thomson, N. R., Clilverd, M. A., & Rodger, C. J. (2017). Midlatitude ionospheric D region: Height, sharpness, and solar zenith angle. *Journal of Geophysical Research: Space Physics*, *122*, 8933–8946. https://doi.org/10.1002/2017JA024455

Thomson, N. R., Clilverd, M. A., & Rodger, C. J. (2018). Quiet daytime arctic ionospheric D region. *Journal of Geophysical Research: Space Physics*, *123*, 9726–9742. https://doi.org/10.1029/2018JA025669

Thomson, N. R., & McRae, W. M. (2009). Nighttime ionospheric *D* region: Equatorial and non-equatorial. *Journal of Geophysical Research*, *114*, A08305. https://doi.org/10.1029/2008JA014001

Thomson, N. R., Rodger, C. J., & Clilverd, M. A. (2011). Daytime *D* region parameters from long-path VLF phase and amplitude. *Journal of Geophysical Research*, *116*, A11305. https://doi.org/10.1029/2011JA016910

Thomson, N. R., Rodger, C. J., & Clilverd, M. A. (2012). Tropical daytime lower D-region dependence on sunspot number. *Journal of Geophysical Research*, *117*, A10306. https://doi.org/10.1029/2012JA018077

Vampola, A. L., & Gorney, D. J. (1983). Electron energy deposition in the middle atmosphere. *Journal of Geophysical Research*, *88*(A8), 6267–6274. https://doi.org/10.1029/JA088iA08p06267

van de Kamp, M., Rodger, C. J., Seppälä, A., Clilverd, M. A., & Verronen, P. T. (2018). An updated model providing long-term data sets of energetic electron precipitation, including zonal dependence. *Journal of Geophysical Research: Atmospheres*, *123*, 9891–9915. https://doi.org/10.1029/2017JD028253

Verronen, P. T., Ulich, T., Turunen, E., & Rodger, C. J. (2006). Sunset transition of negative charge in the D-region ionosphere during high-ionization conditions. *Annales Geophysicae*, *24*, 187–202. https://doi.org/10.5194/angeo-24-187-2006

Wait, J. R., & Spies, K. P. (1964). *Characteristics of the earth-ionosphere waveguide for VLF radio waves* (NBS Tech. Note 300). Boulder, CO: Natl. Bur. of Stand. https://www.govinfo.gov/app/details/GOVPUB-C13-1fc83a916d87542f34917847f89b9f0b